Proceedings of the 2017 IEEE
International Conference on Robotics and Biomimetics
December 5-8, 2017, Macau SAR, China

An Insertable Low-Cost Continuum Tool for Shape Sensing

Kai Xu*, *Member, IEEE*, Yuyang Chen, Zhaoyu Zhang,
Shu'an Zhang, Nianzeng Xing, and Xiangyang Zhu, *Member, IEEE*

***Abstract*—Spatial shape sensing of curved lumens in unknown environments is in great need but challenging. This paper presents the design and experimentation of a low-cost continuum tool that can measure the 3D shapes of internal lumens of a structure, simply by inserting the tool into the lumens. Based on the tool's kinematics model, the shape sensing is achieved by constantly monitoring the outputs on the tool's backbones and the longitudinal motion along the lumen during the insertion. After calibration, the spatial shape of a curved lumen was successfully sensed by the continuum tool. The experimental results demonstrated the effectiveness of the proposed idea.**

I. Introduction

SPATIAL shape sensing of curved internal lumens has drawn quite a bit attention these years, and its applications can be found in various fields, such as inspections in industry and examinations in medicine. The challenge primarily lies on the fact that no direct access is available for measuring the shapes of these internal lumens. Generally, the shape sensing was achieved using various sensors, either internal ones or external ones.

The shape sensing could be achieved by the use of embedded sensors, including Fiber Bragg Grating (FBG) sensors, electromagnetic (EM) sensors, inertial sensors, etc.

FBG sensors were used in shape measurement for colonoscopies, flexible needles and soft manipulators in [1-3]. The reconstructed shape of a manipulator was used for closed-loop control in [4]. Improvements on the use and the specifications of FBG sensors were also attempted. For example, the optimal number and distribution of FGB nodes was discussed in [5], while the torsional rigidity and flexural compliance of FBG fibers' substrate were improved in [6]. The curvature sensing scope of FBG sensors was enlarged in [7]. FBG sensors are advantageous in terms of stability, sensitivity and repeatability. However, the demodulators are usually expensive, particularly when the number of Bragg gratings is increased for measurement over a long range.

EM sensors could be used as well, e.g., to measure the shape of an endoscope in [8]. This approach was improved with extended Kalman filters [9]. Even though the feasibility of shape sensing using EM sensors has been proved, the accuracy highly depends on the positions of the EM sensors in the tracking volume and the curve interpolation algorithms [10, 11]. Moreover, tracking of EM sensors is sensitive to electric/magnetic noises and is not applicable in environments with magnetic materials.

Other embedded sensors can also be found in shape sensing. For example, inertial sensor network was utilized for the shape sensing of colonoscopy robots [12], while PVDF-based (polyvinylidene fluoride) piezoelectric sensors were used for shape sensing of hyper-flexible beams [13]. Signal conditioning and processing are needed for these sensors. The size and wiring complicity also causes trouble for their applications in confined environments.

External sensors for shape sensing are usually from different imaging modalities, such as visual imaging (via the use of one or multiple cameras), radiography and sonography.

Color-based markers were extracted from monocular images to obtain a catheter's planar shape in [14, 15]. Multiple cameras were used to sense the shape of continuum manipulators or to reconstruct the 3-D roadmap of mockup vessel tubes in [16-18]. All the camera-vision-based methods mentioned above either require the placement of multiple cameras to obtain 3-D shapes, or assume a planar bending. Besides, when the lumen for shape sensing is inside a complex structure, it could be impossible to place cameras to take pictures of the outer shapes of the lumen.

Radiography was used for shape sensing of continuum robots, combined with the kinematics model of the robots as in [19, 20]. However, the utilization of X-ray imaging brings the risk of radiation and a high cost associated with the equipment setup.

Sonography is a non-invasive measurement technique. Representative examples include the use of a movable ultrasound transducer to detect the deflection of flexible needles [21], and the algorithm to enhance the accuracy of tubular shape sensing [22]. However, sonography depends on continuous (soft) material distribution for imaging. It would

Manuscript received July 30, 2017. This work was supported in part by the National Natural Science Foundation of China (Grant No. 51435010, Grant No. 91648103 and Grant No. 51375295), and in part by National Key R&D Program of China (Grant No. SQ2017ZY040208).

Kai Xu and Xiangyang Zhu are with the State Key Laboratory of Mechanical System and Vibration, School of Mechanical Engineering, Shanghai Jiao Tong University, Shanghai, 200240, China (asterisk indicates the corresponding author, phone: 8621-34206547; emails: k.xu@sjtu.edu.cn and mexyzhu@sjtu.edu.cn).

Yuyang Chen, Zhaoyu Zhang and Shu'an Zhang are with the RII Lab (Lab of Robotics Innovation and Intervention), UM-SJTU Joint Institute, Shanghai Jiao Tong University, Shanghai, 200240, China (emails: supandoria@sjtu.edu.cn, zhangzhaoyu@sjtu.edu.cn and jimmyonthego@sjtu.edu.cn).

Nianzeng Xing is with the Department of Urology, Beijing Chaoyang Hospital, Capital Medical University, Beijing, China (email: nianzeng2006@vip.sina.com).

978-1-5386-3742-5/17/$31.00 © 2017 IEEE

be nearly impossible to sense the shape of a tube which is suspended within a structure in an industrial setting.

An insertable low-cost continuum tool for shape sensing is hence proposed here, as shown in Fig. 1. It can be used to detect the shape of a curved lumen inside a complex structure or a manipulator with an interior channel. It could find various applications in industrial inspections or medical examinations, where an external imaging modality could hardly detect the shapes of these internal lumens. What's more, the proposed continuum tool does not need expensive equipment that is used in fiber optical demodulation or EM tracking, nor complicated implementation using inertial or PVDF-based piezoelectric sensors.

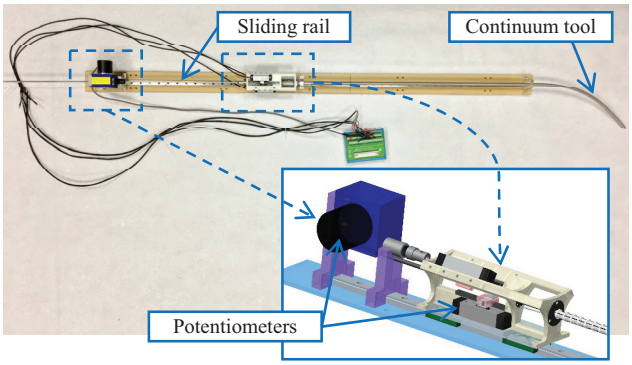

Fig. 1. Design of the continuum tool for shape sensing

This paper is organized as follows. The design concept and working principle of the proposed continuum tool is presented in Section II. The kinematics model and the shape sensing algorithm are presented in detail In Section III. Section IV elaborates the tool's construction and its calibration. The experimental results and analysis are reported in Section V, with conclusions summarized in Section VI.

II. Design Concept and Working Principle

The design concept can be referred to Fig. 2. The continuum tool consists of one base ring, one end ring, many spacer rings, one central tube and three backbones. The rings are fixed to the central tube equidistantly. The backbones are fixed to the end ring. They can slide inside the holes that are arranged on the same pitch circle in the space rings and the base ring. The backbones and the adjacent rings (the base ring, the spacer ring or the end ring) form a segment.

When the continuum tool is inserted into a lumen, it will be bent into the shape of the lumen. Due the back-drivability of the continuum tool, translational outputs (backbone displacements) will be generated. The insertion length and the backbone displacements of the continuum tool are measured by four integrated potentiometers. And the lumen shape would be reconstructed using the kinematics model presented in Section III. An overview of the kinematics model could be explained as follows.

The lumen can be divided into a number of fragments and each fragment can be approximated as an arc with constant curvature, if the division is sufficiently small. When the continuum tool is incrementally inserted, the distal segment of the tool would be bent into the shape of the matching fragment of the lumen. Then the rest of the tool's segments will all be bent from their previous shapes to the current shapes that match their new positions (insertion depth into the lumen). However, this seemingly complicated process is equivalent to stack a new segment on top of the tool while keeping the rest segments unchanged. Length of this newly stacked segment is equivalent to the longitudinal advancement of the continuum tool inside the lumen, while the bending of the newly stacked segment leads to the translational movements of the backbones. Since the insertion length and the backbone movements are measured by the integrated potentiometers, the shape of the newly stacked segment is determined. The shape of the lumen is hence reconstructed by stacking new segments along the tool insertion.

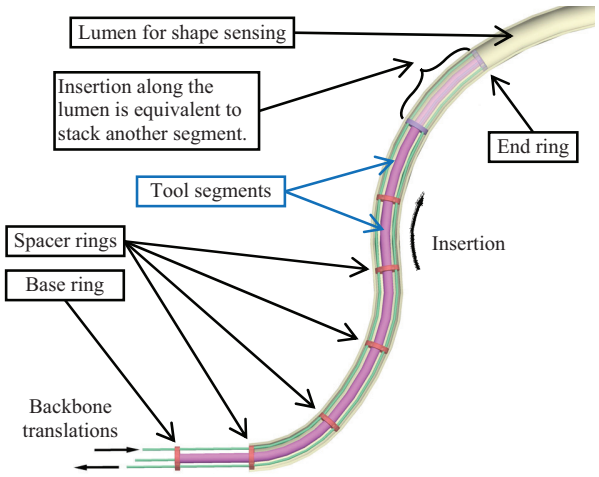

Fig. 2. Working principle of the continuum tool for shape sensing

III. Shape Sensing Kinematics

The shape sensing method is based on the kinematics model of a similar continuum mechanism in [23]. The kinematics of one segment is firstly summarized in Section III.A, while the algorithm for shaping sensing is presented in Section III.B.

A. Kinematics of one Segment

As mentioned in Section II, the continuum tool inside the lumen can be considered to be composed of many segments. Each segment is formed by the backbones and the adjacent rings (the base ring, the spacer ring or the end ring). It is shaped by its matching fragment of the lumen that has constant curvature.

The number of the segments is assumed to be n. The n^{th} segment is the most distal one as shown in Fig. 3. When the t^{th} segment is formed between two spacer rings, the spacer ring which is closer to the base is called the *spacer base ring*, while the other is called the *spacer end ring*.

Four coordinates are attached on the continuum segment:

- *Spacer Base Coordinate*, $\{tb\} = \{\hat{\mathbf{x}}_{tb}, \hat{\mathbf{y}}_{tb}, \hat{\mathbf{z}}_{tb}\}$, is attached to the spacer base ring in the t^{th} segment. $\hat{\mathbf{x}}_{tb}$ points out from the center of the spacer base ring to the first backbone and $\hat{\mathbf{z}}_{tb}$ is normal to the ring.
- *Bending Plane Coordinate 1*, $\{t1\} = \{\hat{\mathbf{x}}_{t1}, \hat{\mathbf{y}}_{t1}, \hat{\mathbf{z}}_{t1}\}$, is attached to the spacer base ring. The continuum segment bends in its XY plane.
- *Bending Plane Coordinate 2*, $\{t2\} = \{\hat{\mathbf{x}}_{t2}, \hat{\mathbf{y}}_{t2}, \hat{\mathbf{z}}_{t2}\}$, is obtained from $\{t1\}$ by a rotation about $\hat{\mathbf{z}}_{t1}$ axis, moving its origin to the center of the t^{th} segment's spacer end ring. $\hat{\mathbf{x}}_{t2}$ axis is normal to the spacer end ring.
- *Spacer End Coordinate*, $\{te\} = \{\hat{\mathbf{x}}_{te}, \hat{\mathbf{y}}_{te}, \hat{\mathbf{z}}_{te}\}$, is attached to the spacer end ring. The $\hat{\mathbf{z}}_{te}$ and $\hat{\mathbf{x}}_{t2}$ axes coincide. $\hat{\mathbf{x}}_{te}$ points from the center to the first backbone.

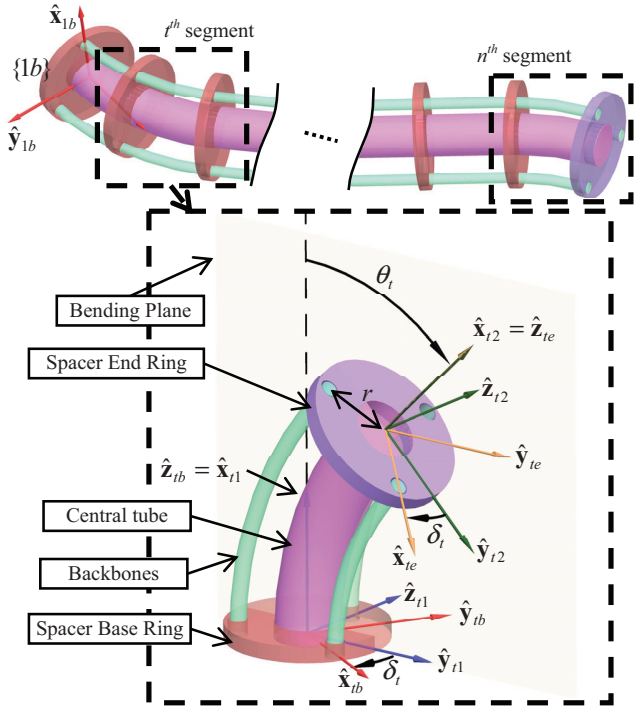

Fig. 3. Nomenclatures and coordinates

The t^{th} segment's central tube bends inside the bending plane. The nomenclature is listed in Table I.

TABLE I
NOMENCLATURE USED IN THIS PAPER

Symbol	Definition
t	Index of the segments, t = 1, 2, 3, …, n.
i	Index of the backbones, i = 1, 2, 3. They are numbered according to the definition of δ_{ti}. Index of the segments always precedes that of the backbones.
r	Distance between a backbone and the ring center.
β	Division angle of the backbones along the pitch circle. $\beta = 2\pi/3$.
θ_t	Bending angle of the t^{th} segment. θ_t is defined as the angle rotating from $\hat{\mathbf{x}}_{t1}$ to $\hat{\mathbf{x}}_{t2}$ in the bending plane.
δ_{ti}	For the t^{th} segment, a right-handed rotation angle from $\hat{\mathbf{y}}_{t1}$ about $\hat{\mathbf{x}}_{t1}$ to a ray passing through the i^{th} backbone.
δ_t	$\delta_t \equiv \delta_{t1}$ and $\delta_{ti} = \delta_t + (i-1)\beta$
L_t, L_{ti}	Lengths of the central tube and the i^{th} backbone in the t^{th} segment, respectively.
q_{ti}	$\boldsymbol{q}_t = [q_{t1}\ \ q_{t2}\ \ q_{t3}]^T$ is the joint actuation length vector for the t^{th} segment. $q_{ti} \equiv L_{ti} - L_t$.
${}^{tb}\mathbf{R}_{te}$	Coordinate transformation matrix from frame $\{te\}$ to frame $\{tb\}$. $\{te\}$ coincides with $\{(t+1)b\}$.
${}^{tb}\mathbf{p}_{te}$	Position vector pointing from the t^{th} spacer base ring center to the center of the t^{th} spacer end ring (namely the spacer base ring in the $(t+1)^{th}$ segment).

The kinematics for the t^{th} segment is summarized as follows, with the derivations available in [23].

$$L_{ti} = L_t + q_{ti} \tag{1}$$

Where $q_{ti} = -r\theta_t \cos\delta_{ti}$.

Eq. (1) can be rewritten as in Eq. (2).

$$\begin{cases} q_{t1} = -r\theta_t \cos\delta_t \\ q_{t2} = -r\theta_t \cos(\delta_t + \beta) \end{cases} \tag{2}$$

Then the mapping for θ_t and δ_t is obtained as follow.

$$\begin{cases} \delta_t = \operatorname{atan2}(q_{t2} - q_{t1}\cos\beta, -q_{t1}\sin\beta) \\ \theta_t = -q_{t1}/r\cos\delta_t \end{cases} \tag{3}$$

The forward kinematics is derived in Eq. (4) and Eq. (5).

$${}^{tb}\mathbf{p}_{te} = \frac{L_t}{\theta_t}\begin{bmatrix} (1-\cos\theta_t)\cos\delta_t \\ (\cos\theta_t - 1)\sin\delta_t \\ \sin\theta_t \end{bmatrix} \tag{4}$$

Where ${}^{tb}\mathbf{p}_{te} = [0\ \ 0\ \ L_t]^T$ when $\theta_t \to 0$.

$${}^{tb}\mathbf{R}_{te} = \mathrm{Rot}(\hat{\mathbf{z}}_{tb}, -\delta_t)\mathrm{Rot}(\hat{\mathbf{z}}_{t1}, \theta_t)\mathrm{Rot}(\hat{\mathbf{z}}_{te}, \delta_t) \tag{5}$$

Where $\mathrm{Rot}(\hat{\mathbf{n}}, \gamma)$ is a rotation matrix about $\hat{\mathbf{n}}$ by an angle γ.

B. Shape Sensing Algorithm

The shape sensing concept is described in Section II. As the continuum tool is inserted into the lumen, the insertion length and the backbone translational outputs are measured by the integrated potentiometers repeatedly. The sampling (a.k.a. measurement) period is 5 milliseconds. The shape of the equivalently stacked segment of the continuum tool is estimated once the tool's potentiometers are read within the sampling cycle.

The reading from the tool's potentiometer for tool insertion represents the total insertion length. It is used to calculate the length of the equivalently stacked segment as in Eq. (6).

$$L_n = \sum_{k=1}^{k=n} L_k - \sum_{k=1}^{k=n-1} L_k \tag{6}$$

Where $\sum_{k=1}^{k=n-1} L_k$ and $\sum_{k=1}^{k=n} L_k$ are the total insertion lengths in the previous and current sampling cycle, respectively.

The readings from the tool's potentiometers for the backbones' translational outputs represent the total actuation lengths. They are used to calculate the actuation lengths of the equivalently stacked segment as in Eq. (7).

$$q_{ni} = \sum_{k=1}^{k=n} q_{ki} - \sum_{k=1}^{k=n-1} q_{ki} \tag{7}$$

Where $\sum_{k=1}^{k=n-1} q_{ki}$ and $\sum_{k=1}^{k=n} q_{ki}$ are the total actuation lengths of the i^{th} backbone in the previous and current sampling cycle, respectively.

With L_n and q_{ni} obtained, θ_n and δ_n could be obtained using Eq. (3). Then ${}^{nb}\mathbf{R}_{ne}$ and ${}^{nb}\mathbf{p}_{ne}$ are obtained using θ_n and δ_n according to Eq. (4) and Eq. (5).

Then the position and orientation of the spacer end ring of the equivalently stacked segment in the base frame $\{1b\}$ are as follows.

$${}^{1b}\mathbf{R}_{ne} = {}^{1b}\mathbf{R}_{nb}\,{}^{nb}\mathbf{R}_{ne} = {}^{1b}\mathbf{R}_{(n-1)e}\,{}^{nb}\mathbf{R}_{ne} \tag{8}$$

$${}^{1b}\mathbf{p}_{ne} = {}^{1b}\mathbf{R}_{nb}\,{}^{nb}\mathbf{p}_{ne} + {}^{1b}\mathbf{p}_{nb} = {}^{1b}\mathbf{R}_{(n-1)e}\,{}^{nb}\mathbf{p}_{ne} + {}^{1b}\mathbf{p}_{(n-1)e} \tag{9}$$

Where $\{(n-1)e\}$ coincides with $\{nb\}$.

The aforementioned process is applied in a recursive way, since the ${}^{(n-1)b}\mathbf{R}_{(n-1)e}$ and ${}^{(n-1)b}\mathbf{p}_{(n-1)e}$ are obtained in the previous sampling cycle, so are the ${}^{1b}\mathbf{R}_{(n-1)e}$ and ${}^{1b}\mathbf{p}_{(n-1)e}$. The spatial shape of the insertable continuum tool is hence reconstructed incrementally. The reconstructed spatial shape represents that of the lumen into which the continuum tool is inserted.

IV. System Construction and Calibration

To verify the efficacy of the proposed shape sensing concept, the insertable continuum tool was fabricated and assembled. The tool was then calibrated to validate the shape sensing experiments presented in Section V.

A. System Construction

The detailed design of this proposed continuum tool is shown in Fig. 4. The tool consists of an insertable portion and a sliding base.

The insertable portion of the continuum tool with a length of 1000 mm and a diameter of 10 mm is shown in Fig. 4(a).

The insertable continuum portion consists of an outer tube, a central tube, three backbones and many spacer rings.

The outer tube has an outer diameter of 10 mm and an inner diameter of 9 mm. It is woven from stainless steels wires and provides a smooth surface for the tool's insertion into a lumen.

The spacer rings have an outer diameter of 9 mm, an inner diameter of 6 mm and a thickness of 2 mm. The central tube has an outer diameter of 6 mm and an inner diameter of 4 mm. Both the central tube and the spacer rings are made from PE (polyethylene). To improve the torsional rigidity of the insertable continuum tool, the spacer rings are fixed onto the central tube via ultrasonic plastic welding.

The backbones are made from super-elastic nitinol rods with a diameter of 0.6 mm. They are spaced 120° apart from each other. The diameter of the pitch circle in which the holes for passing the backbones are arranged is 7.6 mm. The spacer rings are properly aligned to ensure smooth sliding of the backbones before being welded onto the central tube.

The insertable continuum portion is attached to the sliding base of the tool. The sliding base that is fabricated via 3D printing provides housing for three linear potentiometers.

The backbones are extruded into the sliding base to be connected to the three linear potentiometers, passing through three guiding cannulae. The linear potentiometers (KTL-20 from Xiyu electronics Inc. China with an effective travel of 20 mm) are guided by linear slides and measure the translational outputs of the three backbones.

The sliding base is mounted on a linear sliding rail with a length of 1200 mm. A string potentiometer (WXY-30 from Xiyu electronics Inc. China with an effective travel of 1200 mm) is used to measure the translation of the sliding base (a.k.a. the insertion length).

A rigid supporting rod is inserted into the central tube of the tool's insertable portion to keep the continuum portion from slacking under gravity.

Then the sliding base can be manually pushed for inserting the continuum tool into a lumen for shape sensing.

The string potentiometer and the linear potentiometers are connected to a data acquisition card (PCL-818HG from Advantech Inc.). The output voltages of the potentiometers are constantly measured by the card with a sampling period of 5 milliseconds. The A/D converter has a resolution of 12-bit. And the achieved accuracy on the linear potentiometers and the string potentiometer is 9.77×10^{-3} mm and 0.586 mm, respectively.

A MATLAB xPC application is programmed in Simulink and loaded into a Target PC to carry out the data acquisition and the shape sensing, following the algorithm in Section III.B.

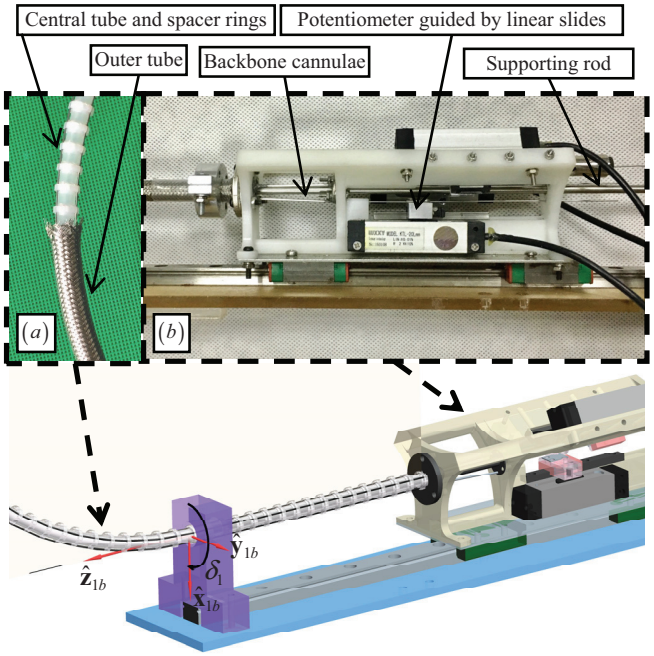

Fig. 4. System description of the insertable continuum tool: (a) the insertable continuum portion, and (b) the 3D printed sliding base

B. *Tool Calibration*

The continuum tool shall be calibrated to ensure that no excessive errors have been introduced during the fabrication and assembling process, in order to verify the proposed idea.

The tool calibration is conducted as shown in Fig. 5. The tool was inserted into a few lumens with known shapes. The circular shapes of these PTFE (polytetrafluoroethylene) lumens are constrained by the geometrical shapes cut on the acrylic boards. Upon an insertion length of 250 mm, the lumen is bent up to 25°, 50° and 75° respectively.

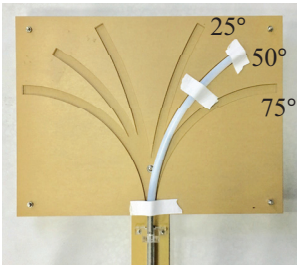

Fig. 5. PTFE lumens with known shapes for the tool calibration

The continuum tool was inserted into the lumens and the readings from the potentiometers were collected. According to the kinematics in Eq. (1), there is an implication as in Eq. (10). This condition indicates that the tool is not extended or compressed. This condition is hence always used to check the integrity of the acquired potentiometer readings.

$$q_{t1} + q_{t2} + q_{t3} = 0 \tag{10}$$

Then the tool was inserted into the lumens and the shape was sensed. The estimated bending angles (cumulated θ_t values) are plotted in Fig. 6. It could be seen from the plot that the sensed angle is approximately proportionally less than the reference value. A calibration coefficient is hence proposed for θ_t as in Eq. (11).

$$\tilde{\theta}_t = c_\theta \theta_t \tag{11}$$

Where $\tilde{\theta}_t$ is the calibrated value for θ_t and c_θ = 1.06. $\tilde{\theta}_t$ should be used in the shape sensing instead of θ_t.

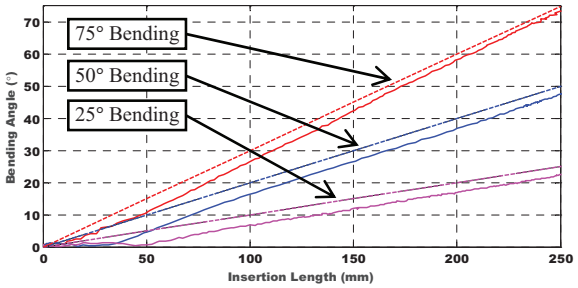

Fig. 6. Results of the tool calibration on the bending angles: dashed lines for the reference values and solid lines for the sensed values

Then the lumen board in Fig. 5 was rotated so that the tool can be inserted into the calibration lumens that were oriented to different directions. The sensed bending direction angles and the reference bending direction angles are plotted in Fig. 7. It could be seen from Fig. 7 that the bending direction angle errors are relative small and vary slightly in different bending directions. The average error is 1.78°. This error might be caused by a fixed twisting angle between the base ring and the end ring, and is compensated by adding a fixed value on δ_t, as in Eq. (12), since the average error is reached for a 250 mm insertion.

$$\tilde{\delta}_t = \delta_t - c_\delta \frac{\sum_{k=1}^{k=t} L_k}{250mm} \tag{12}$$

Where $\tilde{\delta}_t$ is the calibrated value for δ_t and c_δ = 1.78°. $\tilde{\delta}_t$ should be used in the shape sensing instead of δ_t.

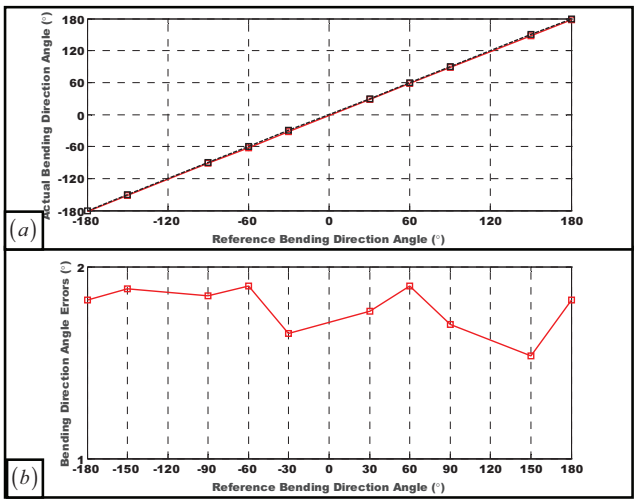

Fig. 7. Results of the tool calibration: (a) bending direction angles, and (b) errors

V. Shape Sensing Experiments

To demonstrate the shape sensing performance of the continuum tool, a spatial PTFE tube is used to simulate a lumen with an unknown shape, as shown in Fig. 8(a).

To fit the size and measurement range of the tool, the lumen for shape sensing has an inner diameter of 10 mm and a total length of 1000 mm. An optical tracker (Micron Tracker SX60, Claron Technology Inc.) was used to obtain the positions of 17 reference points along the lumen to provide a reference shape of the lumen.

The continuum tool for shape sensing was inserted into the lumen five times to show repeatability of the sensed results. The results are plotted in Fig. 8(b).

The errors of the sensed shapes were quantified as follows. For each of the five insertions, the shape curve of the lumen is obtained from a spatial curve fitting with respect to the curve length s ranging from 0 mm to 1000 mm. Then for any s value, there is a point on the curve for each of the five sensed curves. The positions of the five points on the five sensed curves for the same s value were averaged. Then a second curve fitting was conducted using the averaged point positions with respect to the curve length s from 0 mm to 1000 mm.

The maximal distance between the 17 reference points along the lumen measured using the tracker and the averaged shape curve was obtained as the maximal error of the

averaged shape sensing experiments. The error is 15.8mm. This is considered satisfactory given the total length of the lumen (1000 mm).

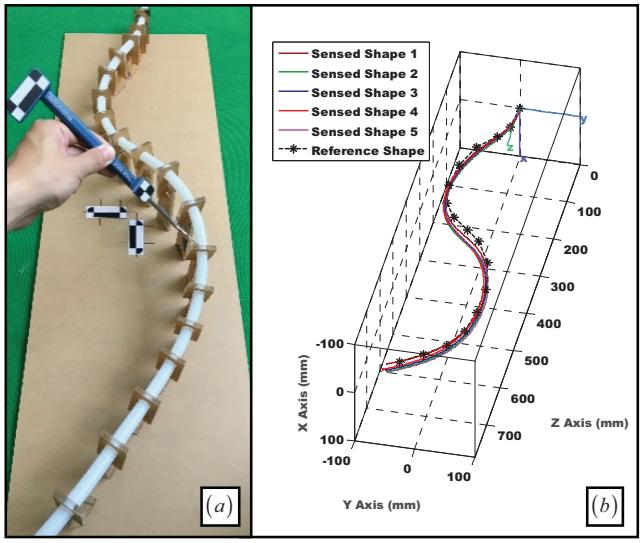

Fig. 8. Experimental validation: (a) the spatial lumen for shape sensing, and (b) the sensed shapes

VI. Conclusion

This paper presents the design, construction, calibration and experimental characterization of an insertable low-cost continuum tool for shape sensing. The fundamental working principle lies on the back-drivability of a multi-backbone continuum mechanism. Based on the kinematics model of the continuum tool that is divided into many continuum bending segments, the shape sensing algorithm is derived.

With proper calibrations, the shape sensing performance of the insertable tool was validated on a lumen with a spatial shape. The continuum tool was inserted into the lumen five times and consistent shape sensing results were obtained. The maximal shape sensing error is about 15.8 mm.

Factors contributing to the shape sensing errors include the backlash in the tool construction (e.g., the tolerances between the backbones and the holes in the spacer rings) and the torsional rigidity of the tool. With the fabrication improved, the tool could be conveniently used for shape sensing of a lumen in an unknown environment or inside a manipulator.

References

[1] L. Zhang, J. Qian, L. Shen, and Y. Zhang, "FBG Sensor Devices for Spatial Shape Detection of Intelligent Colonoscope," in *IEEE International Conference on Robotics and Automation (ICRA)*, 2004, pp. 834-840 Vol.1.

[2] R. J. Roesthuis, M. Kemp, J. J. V. D. Dobbelsteen, and S. Misra, "Three-Dimensional Needle Shape Reconstruction Using an Array of Fiber Bragg Grating Sensors," *IEEE/ASME Transactions on Mechatronics,* vol. 19, pp. 1-12, 2014.

[3] H. Wang, R. Zhang, W. Chen, X. Liang, and R. Pfeifer, "Shape Detection Algorithm for Soft Manipulator Based on Fiber Bragg Gratings," *IEEE/ASME Transactions on Mechatronics,* vol. 21, pp. 2977-2982, 2016.

[4] R. J. Roesthuis and S. Misra, "Steering of Multisegment Continuum Manipulators Using Rigid-Link Modeling and FBG-Based Shape Sensing," *IEEE Transactions on Robotics,* vol. 32, pp. 372-382, 2016.

[5] I. Payo, V. Feliu, and O. D. Cortázar, "Fibre Bragg Grating (FBG) Sensor System for Highly Flexible Single-Link Robots," *Sensors and Actuators A Physical,* vol. 150, pp. 24–39, 2009.

[6] S. C. Ryu and P. E. Dupont, "FBG-Based Shape Sensing Tubes for Continuum Robots," in *IEEE International Conference on Robotics and Automation (ICRA)*, 2014, pp. 3531 - 3537.

[7] L. Hao, A. Farvardin, S. A. Pedram, I. Iordachita, R. H. Taylor, and M. Armand, "Large Deflection Shape Sensing of a Continuum Manipulator for Minimally-Invasive Surgery," presented at the IEEE International Conference on Robotics and Automation (ICRA), 2015.

[8] J. S. Bladen, A. Anderson, G. D. Bell, and D. J. Heatley, "A Non-Radiological Technique for the Real Time Imaging of Endoscopes in 3 Dimensions," in *Nuclear Science Symposium and Medical Imaging Conference*, 1993, pp. 1891-1894 vol.3.

[9] S. Tully, G. Kantor, M. A. Zenati, and H. Choset, "Shape Estimation for Image-Guided Surgery with a Highly Articulated Snake Robot," in *IEEE/RSJ International Conference on Intelligent Robots and Systems (IROS)*, 2011, pp. 1353-1358.

[10] T. Reichl, J. Gardiazabal, and N. Navab, "Electromagnetic Servoing-A New Tracking Paradigm," *IEEE Transactions on Medical Imaging,* vol. 32, p. 1526, 2013.

[11] S. Song, Z. Li, H. Yu, and H. Ren, "Electromagnetic Positioning for Tip Tracking and Shape Sensing of Flexible Robots," *IEEE Sensors Journal,* vol. 15, pp. 4565-4575, 2015.

[12] J. Lee, G. Ukawa, S. Doho, and Z. Lin, "Non Visual Sensor Based Shape Perception Method for Gait Control of Flexible Colonoscopy Robot," in *IEEE International Conference on Robotics and Biomimetics (ROBIO)*, 2011, pp. 577-582.

[13] Y. Shapiro, G. Kósa, and A. Wolf, "Shape Tracking of Planar Hyper-Flexible Beams via Embedded PVDF Deflection Sensors," *IEEE/ASME Transactions on Mechatronics,* vol. 19, pp. 1260-1267, 2014.

[14] R. Reilink, S. Stramigioli, and S. Misra, "Pose Reconstruction of Flexible Instruments from Endoscopic Images Using Markers," in *IEEE International Conference on Robotics and Automation (ICRA)*, 2012, pp. 2938-2943.

[15] J. Back, T. Manwell, R. Karim, and K. Rhode, "Catheter Contact Force Estimation from Shape Detection Using a Real-Time Cosserat Rod Model," in *IEEE/RSJ International Conference on Intelligent Robots and Systems (IROS)*, 2015, pp. 2037-2042.

[16] D. B. Camarillo, K. E. Loewke, C. R. Carlson, and J. K. Salisbury, "Vision Based 3-D Shape Sensing of Flexible Manipulators," in *IEEE International Conference on Robotics and Automation (ICRA)*, 2008, pp. 2940-2947.

[17] J. Jayender, M. Azizian, and R. V. Patel, "Autonomous Image-Guided Robot-Assisted Active Catheter Insertion," *IEEE Transactions on Robotics,* vol. 24, pp. 858-871, 2008.

[18] J. M. Croom, D. C. Rucker, J. M. Romano, and R. J. Webster. III, "Visual Sensing of Continuum Robot Shape Using Self-Organizing Maps," presented at the IEEE International Conference on Robotics and Automation (ICRA), 2010.

[19] E. J. Lobaton, J. Fu, L. G. Torres, and R. Alterovitz, "Continuous Shape Estimation of Continuum Robots Using X-Ray Images," in *IEEE International Conference on Robotics and Automation (ICRA)*, 2013, pp. 725-732.

[20] A. Vandini, C. Bergeles, F. Y. Lin, and G. Z. Yang, "Vision-Based Intraoperative Shape Sensing of Concentric Tube Robots," in *IEEE/RSJ International Conference on Intelligent Robots and Systems (IROS)*, 2015, pp. 2603-2610.

[21] G. J. Vrooijink, M. Abayazid, and S. Misra, "Real-Time Three-Dimensional Flexible Needle Tracking Using Two-Dimensional Ultrasound," in *IEEE International Conference on Robotics and Automation (ICRA)*, 2013, pp. 1688-1693.

[22] H. Ren and P. E. Dupont, "Tubular Enhanced Geodesic Active Contours for Continuum Robot Detection using 3D Ultrasound," in *IEEE International Conference on Robotics and Automation (ICRA)*, 2012, pp. 2907 - 2912.

[23] K. Xu and N. Simaan, "An Investigation of the Intrinsic Force Sensing Capabilities of Continuum Robots," *IEEE Transactions on Robotics,* vol. 24, pp. 576-587, June 2008.